



Cite this: *Dalton Trans.*, 2017, **46**, 10553

Received 31st May 2017,  
Accepted 28th June 2017

DOI: 10.1039/c7dt01970j

rs.c.li/dalton

## Co-Doped $\text{Zn}_{1-x}\text{Cd}_x\text{S}$ nanocrystals from metal–organic framework precursors: porous microstructure and efficient photocatalytic hydrogen evolution†

Xiu Tang,<sup>a</sup> Jia-Hui Zhao,<sup>a</sup> Yu-Han Li,<sup>a</sup> Zi-Ji Zhou,<sup>a</sup> Kui Li,<sup>\*a</sup> Fu-Tian Liu<sup>\*a</sup> and Ya-Qian Lan<sup>id</sup> <sup>\*b</sup>

**Nanoporous Co-doped  $\text{Zn}_{1-x}\text{Cd}_x\text{S}$  were facilely fabricated via adopting ZIFs as templates, and  $\text{Cd}(\text{NO}_3)_2$  and thiourea as precursors. The highly porous microstructure and uniform Co-doping of the photocatalyst afford a high  $\text{H}_2$ -production rate (45.2 and 422.2 times larger than those of  $\text{Zn}_{0.5}\text{Cd}_{0.5}\text{S}$  and  $\text{CdS}$ ), providing an effective way for the development of high performance nanoporous photocatalysts.**

Various nanomaterials,<sup>1–5</sup> particularly inorganic semiconductors,<sup>6–9</sup> are promising for directly transforming solar energy into clean and renewable hydrogen *via* water splitting and were extensively investigated, among which, the metal sulfide semiconductor has been regarded as a promising hydrogen production photocatalyst due to its suitable bandgap ( $E_g$ ) that corresponds to visible light and excellent photocatalytic activity.<sup>10–14</sup> Notably, as the “alloy” of  $\text{ZnS}$  and  $\text{CdS}$ ,  $\text{Zn}_{1-x}\text{Cd}_x\text{S}$ , as a direct band gap semiconductor,<sup>15–18</sup> possesses a continuously tunable lattice constant and bandgap ( $E_g$ ) ranging from 3.66 to 2.4 eV, and better photocatalytic activity than that of single  $\text{CdS}$  and the  $\text{CdS}$  loaded with  $\text{Pt}$  as a cocatalyst.<sup>15,18–21</sup> Among the typical fabrication methods of  $\text{Zn}_{1-x}\text{Cd}_x\text{S}$  solid solution, the wet chemistry method is convenient and simple, but it is still hard to gain the pure phase of  $\text{Zn}_{1-x}\text{Cd}_x\text{S}$  and requires a long reaction time owing to the larger radius of  $\text{Cd}^{2+}$  (0.97 Å) than that of  $\text{Zn}^{2+}$  (0.74 Å).<sup>18,20,22</sup> Moreover, the modulation of the morphology of the  $\text{Zn}_{1-x}\text{Cd}_x\text{S}$  could increase the number of exposed active sites, and enhance the separation and transport efficiency of charge carriers.<sup>20,22,23</sup> Although the organic surfactants were extensively adopted to modulate the morphology of the nanomaterials,

the surfactants inevitably contaminate the heterostructures, and may substantially impair the performance of the heterostructures.<sup>24</sup> Therefore, searching for an efficient surfactant-free hydrothermal method for the synthesis of  $\text{Zn}_{1-x}\text{Cd}_x\text{S}$  solid solution with an improved amount of exposed active sites is an important subject from both theoretical and practical viewpoints.<sup>20</sup>

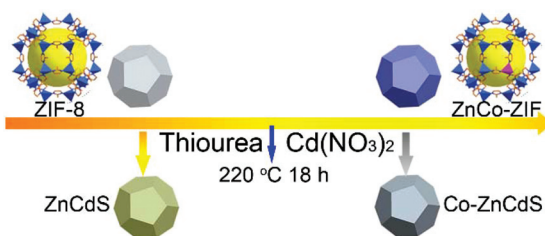
Metal–organic framework (MOF)-templated nanoporous ramifications, such as nanoporous carbons,<sup>25,26</sup> carbide,<sup>27,28</sup> sulfides,<sup>29</sup> phosphide,<sup>30–32</sup> have attracted great attention owing to their extraordinarily high surface areas and the ability to control their pore textures. The main advantage of using a MOF as a template is that the MOF itself works as a precursor and contributes to the formation of high quality nanoporous ramifications. Likewise, fabrication of a MOF-templated photocatalyst with a high surface area could not only increase the exposure of the active sites but also promote the mass transfer and transport of the photo-generated charge carriers.<sup>25,26</sup> Due to their periodic pores and regular architecture, the MOFs could serve as a support to the formation of photocatalysts with the regular architecture and finally generate functional hybrid structures. Moreover, the facile designing of the hybrid MOFs (e.g. Co-doped ZIF-8) could not only vary its pore structure and hence specific surface area,<sup>33</sup> but also adopt the cocatalyst uniformly thanks to the evenly distributed Co in the MOF skeleton.

Herein, various nanoporous  $\text{Zn}_{1-x}\text{Cd}_x\text{S}$  solid solutions were facilely fabricated *via* adopting the zeolitic imidazolate framework (ZIF) as the template and Zn precursors (Scheme 1). Moreover, the quaternary solid solution  $\text{Zn}_{1-x}\text{Cd}_x\text{Co}_y\text{S}$  with Co was distributed evenly around the porous solid solution skeleton by carefully preparing the Co-doped ZIF-8 (ZnCo-ZIF) and using it as the template. Benefiting from its highly porous microstructure, the  $\text{H}_2$ -production rate of the as-prepared solid solutions is dramatically improved. Moreover, the photocatalytic activity of the solid solution was further improved after the doping of Co evenly around the skeleton of the porous solid solution. Under visible light, the photo-

<sup>a</sup>School of Materials Science and Engineering, University of Jinan, Jinan 250022, China. E-mail: mse\_lik@ujn.edu.cn, mse\_liuft@ujn.edu.cn

<sup>b</sup>Jiangsu Key Laboratory of Biofunctional Materials, School of Chemistry and Materials Science, Nanjing Normal University, Nanjing 210023, P. R. China. E-mail: yqlan@njnu.edu.cn

†Electronic supplementary information (ESI) available. See DOI: 10.1039/c7dt01970j



**Scheme 1** Scheme illustrating the synthesis of the  $\text{Zn}_{1-x}\text{Cd}_x\text{S}$  solid solution derived from ZIF precursors.

catalytic hydrogen production rate of  $\text{Zn}_{0.5}\text{Cd}_{0.5}\text{S}$  is as high as  $12.13 \text{ mmol h}^{-1} \text{ g}^{-1}$ , and was further improved to be  $17.36 \text{ mmol h}^{-1} \text{ g}^{-1}$  after the doping of only 0.5 at% Co, which is 45.2 and 422.2 times higher than those of  $\text{Zn}_{0.5}\text{Cd}_{0.5}\text{S}$  (HZC50) and CdS prepared without using MOF as the template. Moreover, this solid solution shows excellent photocatalytic stability over 30 h.

ZIF-8 and ZnCo-ZIF were prepared according to the previous publications using methanol as the solvent, and the X-ray diffraction (XRD) patterns of ZIF-8 and CoZn-ZIF were confirmed as shown in Fig. S1†. A series of samples with a nominal  $\text{Cd}/(\text{Zn} + \text{Cd})$  molar ratio  $x$  are labeled as  $\text{ZC}x$  ( $x = 0, 10, 30, 50, 70$  at%) using the as-prepared ZIF-8 as the template and the Zn precursor to investigate the effect of Cd content on the morphology and photocatalytic activity. ZnCo-ZIF with a uniform Co distribution and different specific surface area was first prepared and used as a template and Zn and Co precursors to prepare the Co-doped optimal solid solution ( $\text{Zn}_{0.5}\text{Cd}_{0.5}\text{S}$ ) samples for making sure the even doping of the solid solution and modulating the morphology of the samples. And the Co-doped  $\text{Zn}_{0.5}\text{Cd}_{0.5}\text{S}$  derived from ZnCo-ZIF with different Co contents ( $y = 0, 0.5, 1$  and 5 at%) were denoted as  $\text{CoZC}y$ . Considering that the wet chemistry method has poor control over the band structure of  $\text{Zn}_{1-x}\text{Cd}_x\text{S}$  and requires a long reaction time owing to the larger radius of  $\text{Cd}^{2+}$  ( $0.97 \text{ \AA}$ ) than that of  $\text{Zn}^{2+}$  ( $0.74 \text{ \AA}$ ),<sup>15,20</sup> and the excellent chemical and thermal stability that ZIF-8 exhibits, it may be difficult to gain the pure  $\text{Zn}_{1-x}\text{Cd}_x\text{S}$  phase. Consequently, the XRD and UV-Vis diffuse reflection spectra were adopted to investigate the phase evolution of the as-prepared  $\text{Zn}_{1-x}\text{Cd}_x\text{S}$  derived from ZIF-8.

Characterization of the phase in  $\text{Zn}_{1-x}\text{Cd}_x\text{S}$  derived from ZIF-8 (Fig. 1a) indicates that only  $\text{Zn}_{1-x}\text{Cd}_x\text{S}$  diffraction peaks could be observed even in the sample with the Cd concentration of only 10 at% (ZC10), which was different from our previous publication.<sup>19</sup> This difference could be explained by the highly porous microstructure of the Zn precursor (ZIF-8), which may facilitate the contact and reaction between the reactive substances, and the formation of the pure solid solution phase even with a low Cd content. In comparison with ZnS, the peak corresponding to  $\text{Zn}_{1-x}\text{Cd}_x\text{S}$  shifted to lower 2-theta values with increasing Cd content, which was consistent with that reported in previous publication.<sup>19,20,22</sup> The Co doping makes the diffraction peaks shift to higher 2-theta values a little bit (Fig. S2†) and no extra diffraction peaks corre-

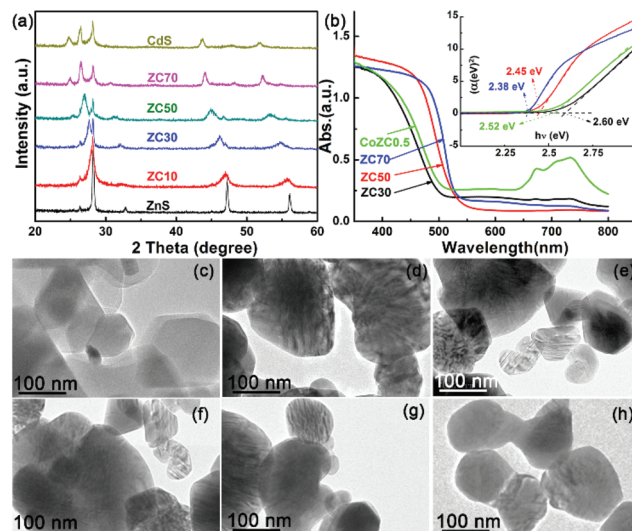


**Fig. 1** Effect of the Cd content on the (a) X-ray diffraction patterns, (b) UV-visible diffuse reflection spectra and band gaps (inset) of the  $\text{Zn}_{1-x}\text{Cd}_x\text{S}$  solid solutions. Transmission electron microscopy (TEM) images of (c) ZIF-8, (d) ZC10, (e) ZC30, (f) ZC50, (g) ZC70, and (h) CoZC0.5, respectively.

ponding to the CoS were observed, indicating the formation of the solid solution phase of  $\text{Zn}_{1-x}\text{Cd}_x\text{Co}_y\text{S}$ . The band edge of the solid solution shifted to longer wavelengths with increasing the Cd content, which is consistent with the XRD results. The effects of the  $\text{Cd}^{2+}$  content on the band structure of the as-prepared were investigated using UV-visible diffuse reflection spectroscopy and were shown in Fig. 1b. The band gap decreased with the increased Cd content. Notably, there are no band edges as reported in the previous  $\text{Zn}_{1-x}\text{Cd}_x\text{S}$  solid solution, and the band gap is a little bit larger than that of the solid solution reported in our previous publication.<sup>19</sup> These results indicate that the highly porous microstructure of the ZIF precursor facilitates the formation of a fairly pure solid solution phase. The Co doping dramatically improved the absorption of visible light (Fig. S3†). Moreover, the inductively coupled plasma (ICP) was further adopted to investigate the composition of the solid solution derived from ZIF-8 (Fig. S4†), no obvious difference between the setting ratio and the testing value was observed.

The adoption of MOF crystals for preparing the nanocatalyst is for the highly porous MOF-templated nanostructure.<sup>25,26,33</sup> Transmission electron microscopy (TEM) was adopted to confirm the MOF-templated porous morphology of the  $\text{Zn}_{1-x}\text{Cd}_x\text{S}$  solid solution (Fig. 1c–h). The ZIF-8 precursor exhibited a porous microstructure with regular block morphology (Fig. 1c). Interestingly, the reaction between  $\text{Cd}^{2+}$  and ZIF-8 showed no dramatic effect on the morphology of the solid solution. The solid solution samples with Cd content ranging from 10 to 70 at% (Fig. 1d–g) exhibited a very similar block morphology to that of the ZIF-8 template, although the block size and the shape of the edge changed a little bit. Likewise, the Co-doped  $\text{Zn}_{1-x}\text{Cd}_x\text{S}$  solid solution by adopting

ZnCo-ZIF as the precursor also possesses the similar morphology to those of the solid solution using ZIF-8 as template (Fig. 1h). These results indicated that ZIF-8 and ZnCo-ZIF not only act as porous precursors but also as templates to modulate the morphology of the as-synthesized  $\text{Zn}_{1-x}\text{Cd}_x\text{S}$  samples.

Nitrogen adsorption/desorption isotherms of the solid solution samples derived from ZIF-8 (ZC50), ZnCo-ZIF (CoZC0.5) and  $\text{Zn}_{0.5}\text{Cd}_{0.5}\text{S}$  (HZC50) derived from  $\text{Zn}(\text{NO}_3)_2 \cdot 6\text{H}_2\text{O}$  are compared in Fig. S5.† Consistent with their similar morphology as confirmed by the TEM results, ZC50 and CoZC0.5 exhibited a large and close specific surface area ( $S_{\text{BET}}$ ), while HZC50 possessed a much smaller specific surface area ( $17.3 \text{ m}^2 \text{ g}^{-1}$ ) without using ZIF-8 as the template. These results further confirmed the important role of ZIF-8 and ZnCo-ZIF for the fabrication of MOF-templated porous nanomaterials. The advantage of the adoption of ZIF crystals as the template was further confirmed by the elemental mapping images (Fig. 2a). Now that the morphology of the ZIF crystals could be well-retained, the Zn site in the template could pin over the whole skeleton, and it acted as the crystallization site for  $\text{Zn}_{1-x}\text{Cd}_x\text{S}$ , which was testified by the uniformly distributed Zn, Cd, and S elements in ZC50 as could be observed from Fig. S6.† Similarly, the introduction of a Co dopant into the MOF-template could make sure of the even distribution of the Co element in the MOF-templated samples, as shown in Fig. 2a. High resolution transmission electron microscopy (HRTEM) was adopted to investigate the phase structure of the as-prepared samples derived from ZIF and ZnCo-ZIF. Both ZC50 and CoZC0.5 (Fig. 2b and c) exhibited a uniform lattice constant corresponding to the solid solution phase, which were consistent with the XRD results.

The hydrogen production activity was selected for the evaluation of the photocatalytic properties of the as-prepared MOF-templated  $\text{Zn}_{1-x}\text{Cd}_x\text{S}$  solid solution. The photocatalytic hydrogen production activity of the  $\text{Zn}_{1-x}\text{Cd}_x\text{S}$  solid solution with different  $\text{Cd}^{2+}$  contents was compared under visible-light

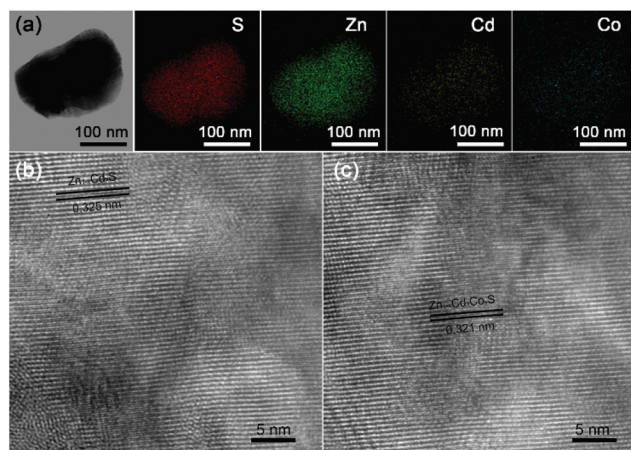


**Fig. 2** Element mapping of CoZC0.5 and HRTEM images of the  $\text{Zn}_{0.5}\text{Cd}_{0.5}\text{S}$ -based solid solutions derived from (b) ZIF-8 and (c) ZnCo-ZIF (Co = 0.5 at%).

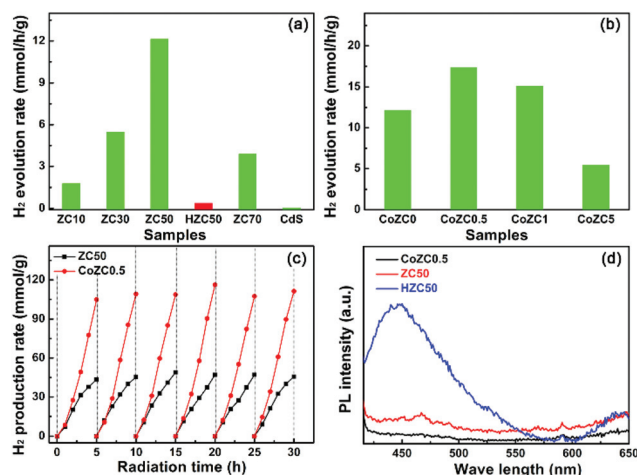


**Fig. 3** The photocatalytic  $\text{H}_2$ -production activities of (a) ZCx samples derived from ZIF-8, and (b) the solid solution doped with different Co contents in a 0.35 M  $\text{Na}_2\text{S}$  and 0.25 M  $\text{Na}_2\text{SO}_3$  mixed aqueous solution under visible-light irradiation. (c) Comparison of the photocatalytic stabilities of ZC50 (square) and CoZC0.5 (circle). (d) The comparison results of the room temperature PL excitation spectra of ZC50 and CoZC0.5.

irradiation ( $\lambda \geq 420 \text{ nm}$ ) (Fig. 3a). In contrast to the negligible visible-light hydrogen evolution activity in mesoporous ZnS (not shown here),<sup>20,22</sup> the production of  $\text{H}_2$  dramatically increased as the content of Cd was increased to 10 at%. Further increases of the amount of Cd led to an increase in the  $\text{H}_2$ -production activity, and ZC50 exhibited the highest  $\text{H}_2$ -evolution rate of  $12.13 \text{ mmol h}^{-1} \text{ g}^{-1}$ . Notably, the MOF-templated ZC50 showed a much larger photocatalytic hydrogen production activity than that of HZC50 due to the highly porous microstructure of ZC50 as confirmed by the TEM and nitrogen adsorption/desorption isotherm measurement. It is well known that only the charge carriers on the surface of the photocatalyst can contribute to the improvement of the photocatalytic activity.<sup>22</sup> The transport distance and the number of exposed active sites are very important for the enhancement of the separation and transport efficiency of electron/hole pairs.<sup>19,20,22</sup> ZC50 shows the shorter transport route compared to that of HZC50 with a much smaller  $S_{\text{BET}}$ . Fig. 3b shows the effect of Co concentration on the photocatalytic activity, the solid solution with 0.5 at% Co-dopant exhibited the maximum hydrogen production rate of  $17.36 \text{ mmol h}^{-1} \text{ g}^{-1}$  (with a quantum efficiency (QE) of 39.2%), which may be attributed to the fact that the doped Co could act as a cocatalyst as extensively reported in previous publications.<sup>34–39</sup> The action spectra of  $\text{H}_2$ -evolution for the samples with different Cd contents derived from ZIF-8 and different Co doping derived from ZnCo-ZIF are shown in Fig. S7.† The MOF-templated solid solutions with porous morphology possessed improved photocatalytic activity and excellent photocatalytic stability over 30 h (Fig. 3c). The similar porous morphology of CoZC0.5 after the photocatalytic reaction over 30 h further confirmed its excellent photocatalytic stability (Fig. S8†).



The photocatalytic activity and the other key parameters of the optimal solid solution with different Cd contents and Co doping were compared and are shown in Fig. S9 and Table S1.† Using the ZIF-8 template and Co-doping, ZC50 and CoZC0.5 exhibited a photocatalytic activity of 32.3 and 46.2 times larger than that of HZC50, respectively. The room temperature PL excitation spectra (Fig. 3d and Fig. S10†) were employed to verify the important role of the MOF-template. HZC50 shows a very strong photoluminescence (PL) peak at around 450 nm, and the relative order of PL response intensity for these samples was found to be: HZC50 > ZC50 > CoZC0.5, which was consistent with the order of the photocatalytic hydrogen evolution activity. Furthermore, the transient photocurrent responses and the electrochemical impedance spectra (EIS) were adopted to confirm the effect of Cd content and Co doping on the separation and transfer of photogenerated charges. The sample with the largest photocatalytic hydrogen activity (ZC50) exhibits the largest photocurrent (Fig. 4a), and the smallest semicircle in the middle-frequency region (Fig. S11†), indicating its faster interfacial electron transfer. The comparison results of the photocurrent and EIS spectra of the solid solution samples derived from ZIF-8 (ZC50), ZnCo-ZIF (CoZC0.5) and  $\text{Zn}_{0.5}\text{Cd}_{0.5}\text{S}$  (HZC50) derived from  $\text{Zn}(\text{NO}_3)_2 \cdot 6\text{H}_2\text{O}$  were carefully evaluated and are listed in Fig. 4b and c. Consistent with the  $\text{H}_2$  evolution tests, the highest photocurrent and smallest semicircle in the middle-frequency region were obtained on CoZC0.5, owing to the synergistic effect of the highly porous microstructure and the Co-dopant. Notably, HZC50 showed a negligible photocurrent and a very large semicircle in the middle-frequency region in comparison with that of ZC50 and CoZC0.5, confirming the importance of MOF-templated highly porous morphology in the process of charge carrier transfer. All the PL excitation spectra, the transient photocurrent responses, and the EIS

spectra confirmed the important role of the MOF template for the synthesis of high-performance photocatalysts of highly porous morphology and even doping. Moreover, the Mott–Schottky plots under dark conditions were also investigated to compare the charge carrier density of the solid solution samples with different Cd contents and Co doping. As could be observed in Fig. 4d, ZC50 with the largest photocatalytic  $\text{H}_2$  evolution rate exhibited the largest charge carrier density among the solid solution with different Cd contents. Notably, there was an obvious upward shift in the flat-band potential after Co doping compared to the pristine one, which is beneficial for the carrier separation.

## Conclusions

Various nanoporous  $\text{Zn}_{1-x}\text{Cd}_x\text{S}$  solid solutions were facilely fabricated *via* adopting the zeolitic imidazolate framework as the template and the Zn precursor. Additionally, the quaternary solid solution  $\text{Zn}_{1-x}\text{Cd}_x\text{Co}_y\text{S}$  with Co was distributed evenly around the porous solid solution skeleton by carefully preparing the ZnCo-ZIF and using it as the template, and Zn and Co precursors, respectively. The highly porous microstructure of the as-prepared solid solution affords a high-efficiency photocatalytic  $\text{H}_2$ -production rate. Meanwhile, the photocatalytic activity of the solid solution was further improved after the doping of Co evenly around the skeleton of the porous solid solution. The photocatalytic hydrogen production rate of  $\text{Zn}_{0.5}\text{Cd}_{0.5}\text{S}$  is as high as  $12.13 \text{ mmol h}^{-1} \text{ g}^{-1}$  under visible light ( $\lambda \geq 420 \text{ nm}$ ), and was further improved to be  $17.36 \text{ mmol h}^{-1} \text{ g}^{-1}$  after the doping of only 0.5 at% Co, which is 45.2 and 422.2 times higher than those of  $\text{Zn}_{0.5}\text{Cd}_{0.5}\text{S}$  and CdS prepared using the similar processing parameters with inorganic  $\text{Zn}(\text{NO}_3)_2 \cdot 6\text{H}_2\text{O}$  as the precursor, respectively. Moreover, this solid solution shows excellent photocatalytic stability over 30 h. The present work provides an effective way for the development of high efficiency nanoporous photocatalysts for  $\text{H}_2$  evolution.

## Acknowledgements

This work was financially supported by the National Natural Science Foundation of Shandong province, China (No. ZR2016BQ26 and ZR2015EL005) and the National Natural Science Foundation of China (NSFC) (No. 21601063).

## Notes and references

- 1 X. Wang, K. Maeda, A. Thomas, K. Takanabe, G. Xin, J. M. Carlsson, K. Domen and M. Antonietti, *Nat. Mater.*, 2009, 8, 76–80.
- 2 J. W. Vickers, H. Lv, J. M. Sumliner, G. Zhu, Z. Luo, D. G. Musaev, Y. V. Geletii and C. L. Hill, *J. Am. Chem. Soc.*, 2013, 135, 14110–14118.

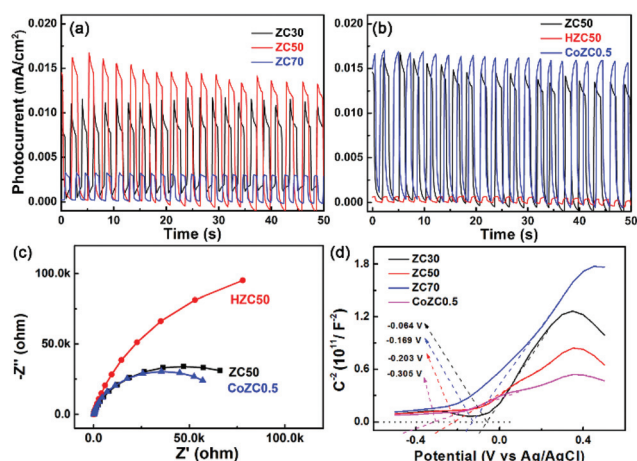


Fig. 4 (a) Effect of Cd concentration on the transient photocurrent responses of the  $\text{ZC}_x$  solid solutions, (b) the transient photocurrent responses and (c) electrochemical impedance spectra of ZC50, HZC50 and CoZC0.5, and (d) the Mott–Schottky plots of the solid solution with different Cd and Co concentrations.

- 3 M. A. Nasalevich, R. Becker, E. V. Ramos-Fernandez, S. Castellanos, S. L. Veber, M. V. Fedin, F. Kapteijn, J. N. H. Reek, J. I. van der Vlugt and J. Gascon, *Energy Environ. Sci.*, 2015, **8**, 364–375.
- 4 J. Wang, C. Li, Q. Zhou, W. Wang, Y. Hou, B. Zhang and X. Wang, *Dalton Trans.*, 2016, **45**, 5439–5443.
- 5 C. Ma, H. Zhu, J. Zhou, Z. Cui, T. Liu, Y. Wang, Y. Wang and Z. Zou, *Dalton Trans.*, 2017, **46**, 3877–3886.
- 6 Z. Zou, J. Ye, K. Sayama and H. Arakawa, *Nature*, 2001, **414**, 625–627.
- 7 X. Chen, S. Shen, L. Guo and S. S. Mao, *Chem. Rev.*, 2010, **110**, 6503–6570.
- 8 F. Zuo, K. Bozhilov, R. J. Dillon, L. Wang, P. Smith, X. Zhao, C. Bardeen and P. Feng, *Angew. Chem., Int. Ed.*, 2012, **51**, 6223–6226.
- 9 M. Li, W. Luo, D. Cao, X. Zhao, Z. Li, T. Yu and Z. Zou, *Angew. Chem., Int. Ed.*, 2013, **52**, 11016–11020.
- 10 Y. Huang, J. Chen, W. Zou, L. Zhang, L. Hu, M. He, L. Gu, J. Deng and X. Xing, *Dalton Trans.*, 2016, **45**, 1160–1165.
- 11 M. K. Jana, U. Gupta and C. N. R. Rao, *Dalton Trans.*, 2016, **45**, 15137–15141.
- 12 J. Zhang, Y. Wang, J. Jin, J. Zhang, Z. Lin, F. Huang and J. Yu, *ACS Appl. Mater. Interfaces*, 2013, **5**, 10317–10324.
- 13 X. Zong, H. Yan, G. Wu, G. Ma, F. Wen, L. Wang and C. Li, *J. Am. Chem. Soc.*, 2008, **130**, 7176–7177.
- 14 K. Li, M. Han, R. Chen, S. L. Li, S. L. Xie, C. Y. Mao, X. H. Bu, X. L. Cao, L. Z. Dong, P. Y. Feng and Y. Q. Lan, *Adv. Mater.*, 2016, **28**, 8906–8911.
- 15 Q. Li, H. Meng, P. Zhou, Y. Zheng, J. Wang, J. Yu and J. Gong, *ACS Catal.*, 2013, **3**, 882–889.
- 16 I. Levchuk, C. Wurth, F. Krause, A. Osvet, M. Batentschuk, U. Resch-Genger, C. Kolbeck, P. Herre, H. P. Steinruck, W. Peukert and C. J. Brabec, *Energy Environ. Sci.*, 2016, **9**, 1083–1094.
- 17 P. P. Wang, Z. B. Geng, J. X. Gao, R. F. Xuan, P. Liu, Y. Wang, K. K. Huang, Y. Z. Wan and Y. Xua, *J. Mater. Chem. A*, 2015, **3**, 1709–1716.
- 18 J. Zhang, J. Yu, M. Jaroniec and J. R. Gong, *Nano Lett.*, 2012, **12**, 4584–4589.
- 19 K. Li, R. Chen, S. L. Li, M. Han, S. L. Xie, J. C. Bao, Z. H. Dai and Y. Q. Lan, *Chem. Sci.*, 2015, **6**, 5263–5268.
- 20 K. Li, R. Chen, S. L. Li, S. L. Xie, X. L. Cao, L. Z. Dong, J. C. Bao and Y. Q. Lan, *ACS Appl. Mater. Interfaces*, 2016, **8**, 4516–4522.
- 21 Y. Yu, J. Zhang, X. Wu, W. Zhao and B. Zhang, *Angew. Chem., Int. Ed.*, 2012, **51**, 897–900.
- 22 K. Li, R. Chen, S. L. Li, S. L. Xie, L. Z. Dong, Z. H. Kang, J. C. Bao and Y. Q. Lan, *ACS Appl. Mater. Interfaces*, 2016, **8**, 14535–14541.
- 23 Y. Huang, Y. Xu, J. Zhang, X. Yin, Y. Guo and B. Zhang, *J. Mater. Chem. A*, 2015, **3**, 19507–19516.
- 24 Y. P. Xie, Z. B. Yu, G. Liu, X. L. Ma and H.-M. Cheng, *Energy Environ. Sci.*, 2014, **7**, 1895–1901.
- 25 J. S. Li, Y. Y. Chen, Y. J. Tang, S. L. Li, H. Q. Dong, K. Li, M. Han, Y. Q. Lan, J. C. Bao and Z. H. Dai, *J. Mater. Chem. A*, 2014, **2**, 6316–6319.
- 26 J. S. Li, S. L. Li, Y. J. Tang, K. Li, L. Zhou, N. Kong, Y. Q. Lan, J. C. Bao and Z. H. Dai, *Sci. Rep.*, 2014, **4**, 5130–5138.
- 27 J. S. Li, Y. J. Tang, C. H. Liu, S. L. Li, R. H. Li, L. Z. Dong, Z. H. Dai, J. C. Bao and Y. Q. Lan, *J. Mater. Chem. A*, 2016, **4**, 1202–1207.
- 28 J. S. Li, Y. Wang, C. H. Liu, S. L. Li, Y. G. Wang, L. Z. Dong, Z. H. Dai, Y. F. Li and Y. Q. Lan, *Nat. Commun.*, 2016, **7**, 11204–11208.
- 29 B. Ma, P. Y. Guan, Q. Y. Li, M. Zhang and S. Q. Zang, *ACS Appl. Mater. Interfaces*, 2016, **8**, 26794–26800.
- 30 S. H. Ahn and A. Manthiram, *J. Mater. Chem. A*, 2017, **5**, 2496–2503.
- 31 J. Yang, F. J. Zhang, X. Wang, D. S. He, G. Wu, Q. H. Yang, X. Hong, Y. Wu and Y. D. Li, *Angew. Chem., Int. Ed.*, 2016, **55**, 12854–12858.
- 32 L. Jiao, Y. X. Zhou and H. L. Jiang, *Chem. Sci.*, 2016, **7**, 1690–1695.
- 33 Y. Z. Chen, C. M. Wang, Z. Y. Wu, Y. J. Xiong, Q. Xu, S. H. Yu and H. L. Jiang, *Adv. Mater.*, 2015, **27**, 5010–5016.
- 34 J. Wang, B. Li, J. Z. Chen, N. Li, J. F. Zheng, J. H. Zhao and Z. P. Zhu, *Appl. Surf. Sci.*, 2012, **259**, 118–123.
- 35 L. J. Zhang, R. Zheng, S. Li, B. K. Liu, D. J. Wang, L. L. Wang and T. F. Xie, *ACS Appl. Mater. Interfaces*, 2014, **6**, 13406–13412.
- 36 Z. Li, Y. Q. Wu and G. X. Lu, *Appl. Catal., B*, 2016, **188**, 56–64.
- 37 J. R. Wang and F. E. Osterloh, *J. Mater. Chem. A*, 2014, **2**, 9405–9411.
- 38 X. X. Chang, T. Wang, P. Zhang, J. J. Zhang, A. Li and J. L. Gong, *J. Am. Chem. Soc.*, 2015, **137**, 8356–8359.
- 39 B. Tian, W. L. Zhen, H. B. Gao, X. Q. Zhang, Z. Li and G. X. Lu, *Appl. Catal., B*, 2017, **203**, 789–797.